J Mater Sci: Mater Electron (2023) 34:803

Bi_2O_3-B_2O_3-CaF_2-EuF_3 glass–ceramics for lighting applications

B. C. Jamalaiah[1,*], N. Madhu[2], Shaik Annar[3], K. Venkata Rao[4], and K. Pavani[5]

[1] Department of Physics, Rajeev Gandhi Memorial College of Engineering and Technology (Autonomous), Nandyal 518501, Andhra Pradesh, India
[2] Department of Physics, P.R.R. & V.S. Government Degree College, Vidavaluru 524318, Andhra Pradesh, India
[3] Department of Chemistry, M.R.R. Government Degree College, Udayagiri 524226, Andhra Pradesh, India
[4] Department of Physics, Government Degree College, Porumamilla 516193, Andhra Pradesh, India
[5] I3N, Department of Physics, University of Aveiro, 3810-139 Aveiro, Portugal

Received: 6 December 2022
Accepted: 4 March 2023

ABSTRACT

The Bi_2O_3-B_2O_3-CaF_2-EuF_3 (BiBCEu) glass and glass–ceramics were prepared by controlled heat treatment method for orange-red laser sources and characterized through X-ray diffraction, Fourier transform infrared, Raman, transmission electron microscopy, photoluminescence excitation, emission and luminescence decay studies. Up on 396 nm excitation, the BiBCEu glass–ceramics containing $Bi_3B_5O_{12}$ and CaF_2 nanocrystallites exhibit an enhanced orange-red luminescence through Eu^{3+}:$^5D_0 \rightarrow {}^7F_2$ (616 nm) transition. The radiative parameters such as radiative emission probability rate (A_R), luminescence branching ratio (β_R) and radiative decay time (τ_R) were determined using the intensities of Eu^{3+}: $^5D_0 \rightarrow {}^7F_J$ (J = 1, 2, 4) emission transitions following the Judd–Ofelt theory. The chromaticity coordinates of BiBCEu glass–ceramic heat treated at 575 °C for 10 h are situated in the orange-red region of the CIE diagram. The BiBCEu glass–ceramic synthesized at 575 °C for 10 h has an excellent proficiency for solid state orange-red laser sources.

1 Introduction

The oxyfluoride glass–ceramics (GCs) doped with certain rare earth (RE) ions and having one or more crystalline phases distributed uniformly within the glassy phase have been the significant materials for various optical applications owing to their intense and narrow emission lines, high luminescence efficiency and long decay time [1–3]. The transparent GCs having low optical absorption and scattering losses with relative refractive index difference between the glassy and crystalline phases of the order 0.1 can be fabricated by modifying the experimental conditions. The refractive index is found higher in GCs compared to that of bared glasses and it increase with the increase of annealing time [4]. The

Address correspondence to E-mail: bcjphysics@gmail.com; jamalaiahbc@rgmcet.edu.in

https://doi.org/10.1007/s10854-023-10218-y
Published online: 22 March 2023

importance of borate based host matrix containing Bi_2O_3 heavy metal oxide, the formation of $Bi_3B_5O_{12}$ and CaF_2 nanocrystallites have been clearly discussed in our earlier research work [5]. It is well known that GCs are polycrystalline materials in which the crystallites are dispersed uniformly throughout the glassy matrix. The GCs are characterized through their high strength, high impact resistance, considerably low thermal expansion coefficient, excellent translucent properties and thermal shock resistance. They can be synthesized through controlled crystallization of base glass. They are resistant to surface damage due to its improved tensile strength and they have a low thermal coefficient of expansion. These qualities favour GCs to be used in many industrial, scientific, defense and bio-medical fields. The GCs find applications in solar panels, liquid crystal display devices, high-temperature lamp envelops, magnetic disc substrates and smart electronic devices.

Trivalent europium (Eu^{3+}) is one of the best and efficient RE ions used for efficient red and/or orange-red colour center in optical devices due to its dominant emission through $^5D_0 \rightarrow {}^7F_2$ transition. The Eu^{3+} ions have been used to probe the site symmetry as well as inhomogeneity of the ligand environment due to the non-degenerate $^7F_0$ ground and $^5D_0$ excited states and relatively simple energy level system [6, 7]. The laser characteristic parameters such as radiative emission probability (A_R), luminescence branching ratio (β_R) and radiative decay time (τ_R) have been evaluated using the intensities of Eu^{3+}: $^5D_0 \rightarrow {}^7F_J$ (J = 1, 2, 4) emission transitions following the Judd–Ofelt (J-O) theory [8, 9]. In literature, the Eu^{3+} -doped various multi-composition GCs have been reported for different optical, sensor and photonic applications [10–12]. This research work reports the synthesis, morphological, structural and optical analysis of 1.0 mol% Eu^{3+} activated Bi_2O_3-B_2O_3-CaF_2 glass and GCs. The process of finding the three phenomenological J-O intensity parameters (Ω_2, Ω_4 and Ω_6) using the Eu^{3+}: $^5D_0 \rightarrow {}^7F_{J\,=\,1,2,4,6}$ emission transitions is also presented.

2 Experiments

2.1 Preparation

The glass samples of composition, 71.25 Bi_2O_3 + 17.75 B_2O_3 + 10.00 CaF_2 + 1.00 EuF_3 (in mol%) were prepared by conventional melt quench method. High purity Bi_2O_3 (99%), H_3BO_3 (99.5%), CaF_2 (99.99%) and EuF_3 (99.99%) were used as precursors. A batch composition of about 20.0 g homogeneous powder with an additional amount of 5.0 wt% of H_3BO_3 (to compensate its loss at higher temperatures) was taken and heat treated at 300 °C for 5 h, cooled to room temperature and then grinded into a fine powder in dust free environment. These heat treated powders were melted for 30 min using a pre-heated muffle furnace at 1000 °C at ambient pressure and air-quenched in a clean atmosphere, then annealed at 400 °C for 20 h to eliminate thermal strains developed during the process of quenching. The as-prepared glasses were heat treated at 575 °C for 5 h and 10 h to continue the crystallization process forming $Bi_3B_5O_{12}$ and CaF_2 nanocrystallites and hence to obtain transparent GCs. The prepared samples were labeled as BiBCEu-G (as prepared glass), BiBCEu-GC1 (heat treated at 575 °C for 5 h) and BiBCEu-GC2 (heat treated at 575 °C for 10 h).

2.2 Characterization

The powder X-ray diffraction (PXRD) patterns were recorded using Rigaku Miniflex 600 X-ray Diffractometer ($\lambda_{CuK\alpha}$ = 1.5406 Å). The Fourier transform infrared (FT-IR) and Raman analysis were carried out with Perkin Elmer Spectrum One Spectrometer (KBr pellet) and Horiba Micro-Raman Spectrometer provided with 532 nm laser, respectively. The formation of $Bi_3B_5O_{12}$ and CaF_2 nanocrystallites was examined with a JEM 2100 plus Hi-Resolution Transmission Electron Microscope (HR-TEM). The room temperature absorption studies were carried out on Perkin Elmer Lambda 950 Spectrophotometer. The photoluminescence excitation, visible emission and fluorescence decay studies were carried out with Jobin YVON Fluorolog-3 Spectrofluorimeter. All the characterizations were done at normal conditions only.

3 Results and discussion

3.1 Structure and morphology

The PXRD patterns of BiBCEu-G and GCs are illustrated in Fig. 1. The PXRD profile of BiBCEu-G reveals pure amorphous phase while BiBCEu-GC1 and BiBCEu-GC2 samples show a combined phase of

glass and crystalline. From these profiles, one can know that the PXRD profile of BiBCEu-GC2 is similar to the previous work on BiBCEr-GCs [5] and it contains crystalline peaks corresponding to the $Bi_3B_5O_{12}$ (JCPDS No. 00–025-1089) and CaF_2 (JCPDS No. 00-001-1274) nanocrystallites. The PXRD peaks noticed at around 2θ = 27.86, 47.02 and 55.61 have been ascribed to (111), (220) and (311) crystal planes of CaF_2.

The FT-IR spectral profiles of BiBCEu-G, BiBCEu-GC1 and BiBCEu-GC2 samples shown in Fig. 2 are almost identical and they reveal seven IR absorption bands with considerably small shift towards longer wavenumber region with increase of crystallanity due to heat treatment. The FTIR bands positioned at around (3465.2–3466.2), (1339.1–1340.4), (1222.2–1223.1), (1084.9–1086.0), (921.6–922.6), (684.1–685.2) and (532.9–534.1) cm^{-1} have been ascribed to symmetric stretching vibrations of OH^- group, asymmetric stretching vibrations of B-O bonds, B-O stretching vibrations in BO_3 units, B-O stretching vibrations in BO_4 units, bending vibrations of B-O-B linkage and Bi-O bending vibration in BiO_6 units, respectively [13–17]. These results are identical to those reported for Er^{3+} doped Bi_2O_3-B_2O_3 glass–ceramics [5].

The Raman spectral profiles of BiBCEu-G, BiBCEu-GC1 and BiBCEu-GC2 samples in the Raman shift range 50–950 cm^{-1} are also identical and they are shown in Fig. 3. Like FTIR bands, the Raman band positions are also shift towards higher wavenumber region with increase of crystallanity due to heat treatment. The Raman bands are positioned at around (128.1–129.2), (154.0–155.6), (277.9–279.0), (336.0–337.5), (691.2–692.3) and (757.6–758.4) cm^{-1}.

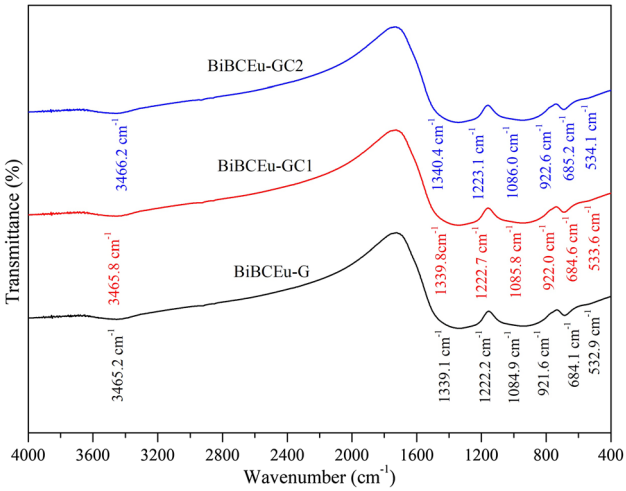

Fig. 2 FT-IR spectral profiles of BiBCEu-G and GCs

The Raman band positions in the region 128.1–337.5 cm^{-1} confirm the formation of CaF_2 nanocrystallites [18, 19], while the Raman bands noticed in the region 691.2–758.4 cm^{-1} corresponds to $Bi_3B_5O_{12}$ nanocrystallites [20, 21].

The realization of nanocrystallites alongside the glassy phase has also been examined from the TEM image of BiBCEu-GC2 and it is shown in Fig. 4a. This image shows a uniform distribution of nanocrystallites. The lattice spacing corresponding to (111) crystal plane [$d_{(111)}$] is estimated to be 0.318 nm using HR-TEM micrograph shown in Fig. 4b and it is close to CaF_2 nanoparticles [22]. The selected area electron diffraction (SAED) image has been used to find the (h k l) crystal planes. It is well known that the $d_{(hkl)}$ is equal to the reciprocal of radius of SAED ring. The

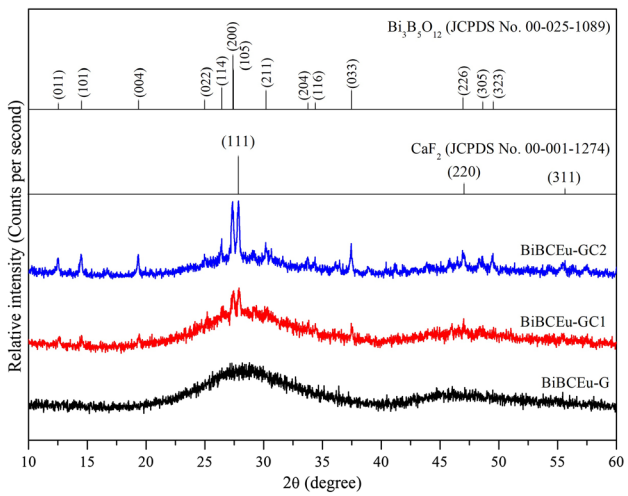

Fig. 1 PXRD profiles of BiBCEu-G and GCs

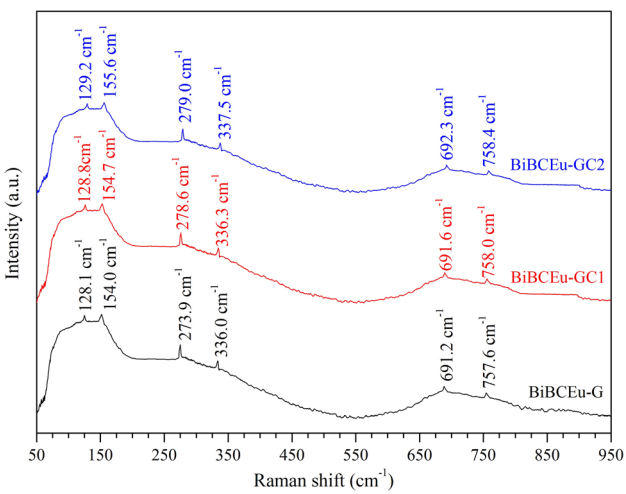

Fig. 3 Raman spectral profiles of BiBCEu-G and GCs

observed SAED rings have been ascribed to (111) (220) and (311) lattice planes of CaF_2 nanoparticles and they are described in Fig. 4c.

It is well known that the fluoride nanocrystals facilitate low phonon energy environments for RE ions and the glasses and GCs with good transparency and relatively low phonon energy could be an attractive material for numerous photonic appliances. The addition of F^- reduce the phonon energy and hence the OH^- content resulting to enhance the luminescence properties of RE ions [23]. J.L Adam et al. [24] reported that the thermal stability of amorphous materials improves with the addition of F^-. The channel waveguide materials based on fluoride and oxyfluoride glasses were prepared with 0.3 dB/cm background loss and 1 dB/cm net gain at 1.5 μm for integrated optical components [25]. These reports reveal that the presence of F^- content can enhance the thermal and optical properties by minimizing background losses. The formation and characteristic behaviour of CaF_2 nanocrystals in oxyfluoride glasses for various photonic applications were reported [3]. The phonon energy of oxide based bismuth borate glass is about 1466 cm^{-1} [26]. In the

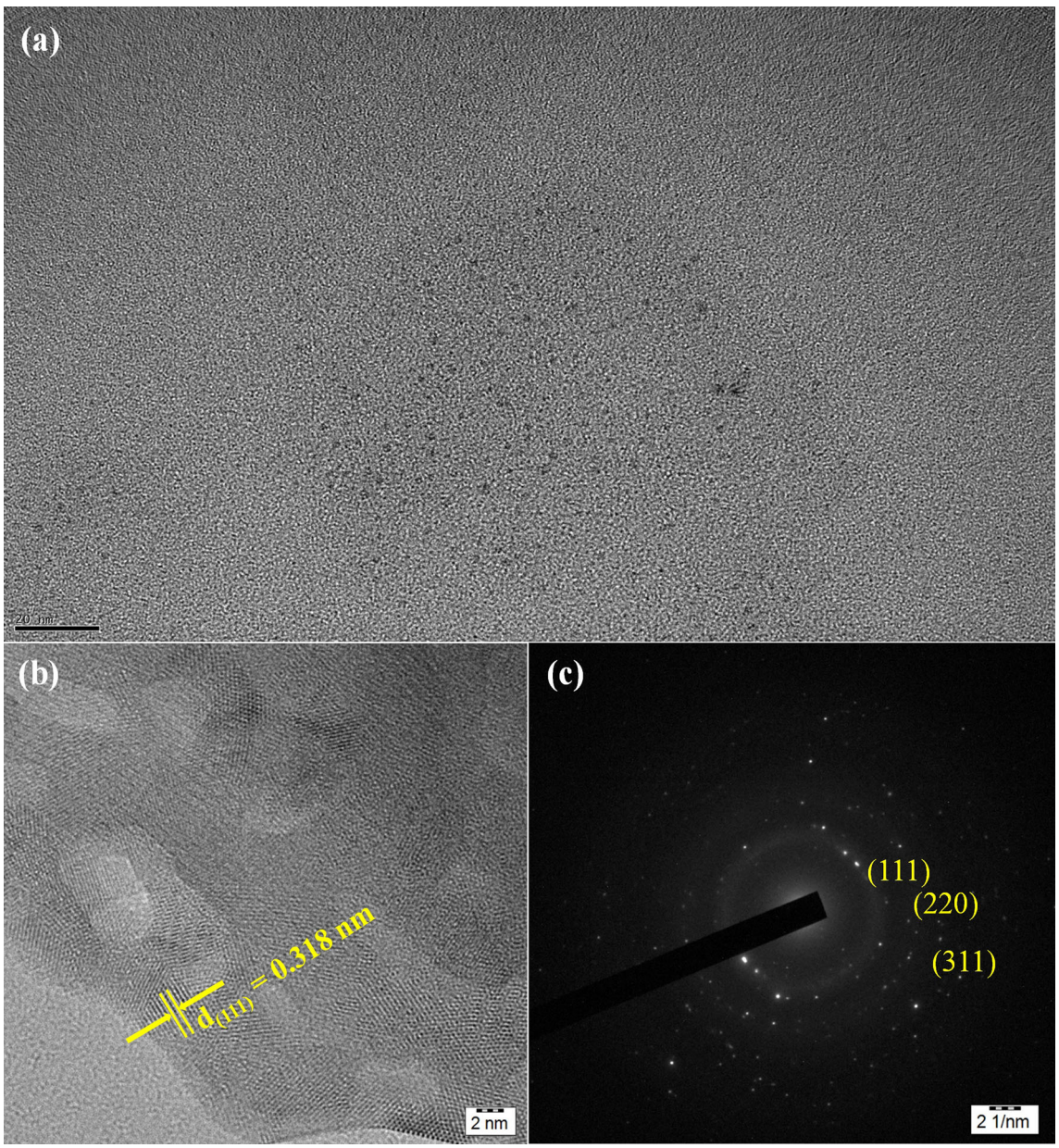

Fig. 4 TEM (**a**), HR-TEM (**b**) and SAED (**c**) images of BiBCEu-GC2

present investigation, the inclusion of fluorine amount significantly lowers the phonon energy of Bi_2O_3-B_2O_3 glass system and it is obtained as 1334.67 ± 0.93 cm^{-1} [5].

3.2 Near UV–VIS absorption spectra

The near UV–VIS optical absorption spectra of BiBCEu-G and GCs in the wavelength range from 375 to 600 nm are shown in Fig. 5. The inset-(a) of Fig. 5 illustrates the magnified spectral region from 500 to 600 nm. These spectra reveal two groups of very weak absorption bands originating from the $^7F_0$ ground energy state and the $^7F_1$ first excited energy state. The observed absorption bands have been attributed to the $^7F_0 \rightarrow {}^5L_6$ (about 395 nm), $^7F_0 \rightarrow {}^5D_3$ (about 420 nm), $^7F_0 \rightarrow {}^5D_2$ (about 465 nm), $^7F_0 \rightarrow {}^5D_1$ (about 525 nm), $^7F_1 \rightarrow {}^5D_1$ (about 537 nm), $^7F_0 \rightarrow {}^5D_0$ (about 579 nm) and $^7F_1 \rightarrow {}^5D_0$ (about 590 nm) transitions [27]. The presence of these absorption transitions is an indication for the uniform distribution of Eu^{3+} ions in BiBCEu-G, BiBCEu-GC1 and BiBCEu-GC2 samples. Usually, the presence of surface defects (if any) results a broadening of absorption band. In the present research work, the broadening of absorption bands is almost negligible indicating fever surface defects due to the crystallization effect by the heat treatment. From these spectra it is obvious that the absorbance of the samples reduce with the enhancement of crystallization of $Bi_3B_5O_{12}$ and CaF_2 nanocrystallites. The inset-(b) of Fig. 5 illustrates the variation of absorbance of $^7F_0 \rightarrow {}^5D_2$ transition with crystallization. In general, Eu^{3+} ions in any host matrix exhibit very weak absorption transitions in near UV–VIS region [4, 11, 28]. In case of Eu^{3+} ions, the estimation of oscillator strengths and hence the J-O intensity parameters become difficult using near UV–VIS absorption spectra. However, the absorption spectral profiles have been used to evaluate optical band gap energies of BiBCEu-G and GCs.

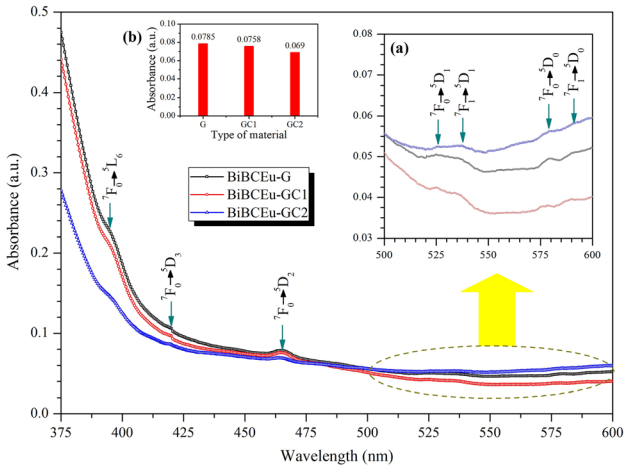

Fig. 5 UV–VIS absorption spectra of BiBCEu-G and GCs. Insets show the magnified spectral region from 500–600 nm (**a**) and the variation of absorbance of $^7F_0 \rightarrow {}^5D_2$ transition with crystallization (**b**)

In order to know the suitability of a luminescent material for an optical application, the knowledge of its optical band gap energy (E_g) is essential and it is expressed in terms of photon energy (hν) and the fundamental absorption edge coefficient (α) as $\alpha . (h\nu) = B(h\nu - E_g)^r$, where B is the energy independent parameter. The parameter r is 1/2 for direct allowed, 1/3 for direct forbidden, 2 for indirect allowed and 3 for indirect forbidden transitions [29]. The $(\alpha.h\upsilon)^2$ vs $h\upsilon$ plots are known as the Tauc's curves. When the linear region of Tauc's curve is extrapolated to $(\alpha.h\upsilon)^2 = 0$, then the corresponding energy is known as direct allowed E_g. The values of E_g are obtained as 2.820, 2.444 and 2.183 (± 0.01) eV for BiBCEu-G, BiBCEu-GC1 and BiBCEu-GC2, respectively from the Tauc's plots for $r = 1/2$ illustrated in Fig. 6. Similar kind of results have been reported for Eu^{3+}-doped $BaBi_2Ta_2O_9$ based glass–ceramics in which the value of direct band gap energy decreases from 2.82 eV for as prepared glass to 1.62 eV for GC heat treated at 550 °C for 12 h [30]. For Eu^{3+} -doped zinc silicate derived from waste rice husks, the direct band gap energy value varies from 4.14 eV for a glass to 3.71 eV for GC heat treated at 1000 °C for 3 h [31]. For Er^{3+} -doped GBANZ glass–ceramics, the direct band gap energy value changes from 3.7750 eV for glass to 3.5220 eV for GC heat treated at 595 °C for 1 h [32]. The gradual reduction in E_g value with increase of crystallization time could be due to the presence of unoccupied energy states below the conduction band edge which causes a structural modification around the Eu^{3+} ions.

3.3 Luminescence analysis

The photoluminescence excitation (PLE) spectra of BiBCEu-G and GCs monitoring the emission corresponding to Eu^{3+}: $^5D_0 \rightarrow {}^7F_2$ (616 nm) transition are shown in Fig. 7. These spectra reveal a total of nine PLE bands due to $^7F_0 \rightarrow {}^5D_4$ (about 363 nm),

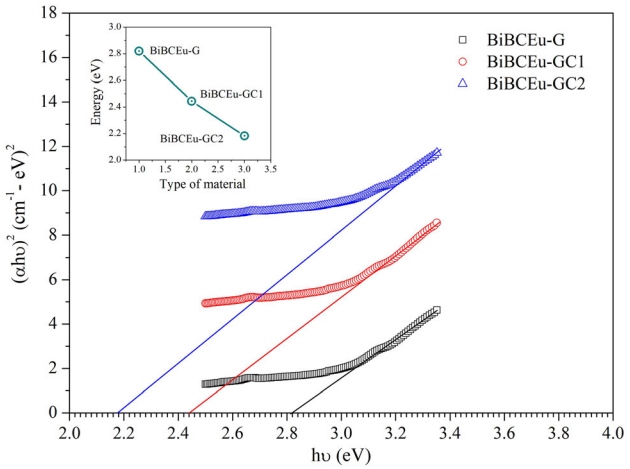

Fig. 6 Tauc's plots for direct allowed transitions for BiBCEu-G and GCs. Inset shows the variation of band gap energy as a function of crystallization

$^7F_0 \rightarrow {}^5G_2$ (about 383 nm), $^7F_0 \rightarrow {}^5L_6$ (about 396 nm), $^7F_0 \rightarrow {}^5D_3$ (about 416 nm), $^7F_0 \rightarrow {}^5D_2$ (about 466 nm), $^7F_0 \rightarrow {}^5D_1$ (about 527 nm), $^7F_1 \rightarrow {}^5D_1$ (about 534 nm), $^7F_0 \rightarrow {}^5D_0$ (about 579 nm) and $^7F_1 \rightarrow {}^5D_0$ (about 589 nm) transitions [27]. The imperfections caused by the crystallization process with heat treatment have no considerable influence on peak maxima of observed PLE bands due to the availability of number of vibrational levels. However, the strength and/or intensity of PLE bands improve with the enhancement of crystallization without causing any shift in their peak maxima. The inset of Fig. 7 describes the variation of strength of $^7F_0 \rightarrow {}^5L_6$ (396 nm) transition as a function of crystallization. From the PLE spectra one can notice that the BiBCEu-GC2 exhibits prominent and high intensity emission bands than the other glass and GC samples. It could be due to the more crystalline atmosphere around the Eu^{3+} ions. The prominent excitation band noticed at 396 nm (Eu^{3+}: $^7F_0 \rightarrow {}^5L_6$) indicates that the studied BiBCEu-G and GCs can show an efficient luminescence when excited at 396 nm radiation.

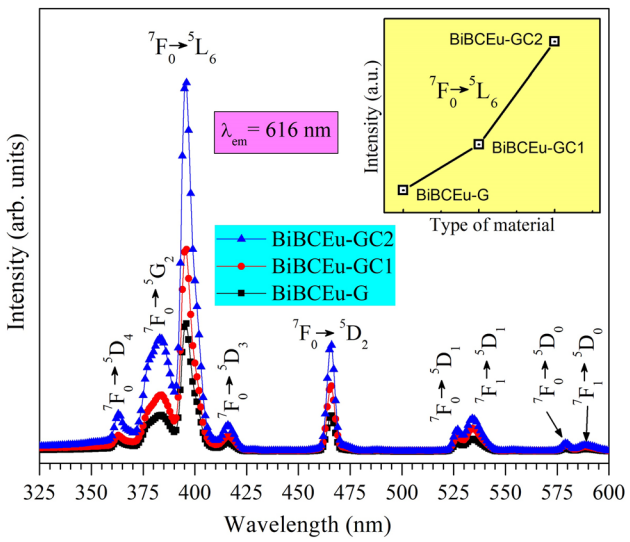

Fig. 7 Photoluminescence excitation spectra (λ_{em} = 616 nm) of BiBCEu-G and GCs. Inset shows the variation of intensity of $^7F_0 \rightarrow {}^5L_6$ (396 nm) transition as a function of crystallization

Upon 396 nm excitation, the emission spectra of BiBCEu-G and GCs in the spectral range from 550 to 750 nm are presented in Fig. 8. The emission spectra displayed a total of five emission bands at 580, 594, 616, 653 and 700 nm and they are assigned to Eu^{3+}: $^5D_0 \rightarrow {}^7F_0$, Eu^{3+}: $^5D_0 \rightarrow {}^7F_1$, Eu^{3+}: $^5D_0 \rightarrow {}^7F_2$, Eu^{3+}: $^5D_0 \rightarrow {}^7F_3$ and Eu^{3+}: $^5D_0 \rightarrow {}^7F_4$ transitions, respectively. From these spectra it is known that the BiBCEu-GC2 sample exhibits intense luminescence when excited at 396 nm radiation. From the emission spectral profiles one can notice a negligible red shift in emission band positions towards longer wavelength regions. This red shift is mainly due to the presence of crystal imperfections caused by the different heat treatment processes. The observed E_g values of 2.820, 2.444 and 2.183 (± 0.01) eV for BiBCEu-G, BiBCEu-GC1 and BiBCEu-GC2, respectively support these results. The inset of Fig. 8 illustrates the emission mechanism of Eu^{3+} in BiBCEu-G and GCs. The process of emission of Eu^{3+} ions in BiBCEu-G and GCs takes place as follows.

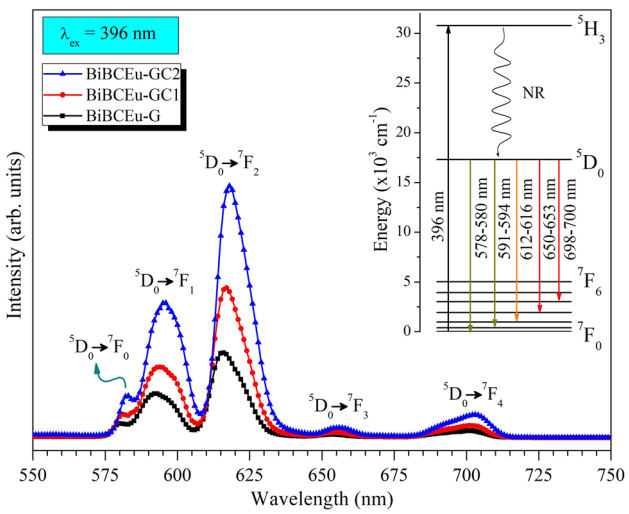

Fig. 8 Emission spectra (λ_{ex} = 396 nm) of BiBCEu-G and GCs. Inset shows the partial energy level diagram of Eu^{3+} ions

Up on pumping at 396 nm wavelength, the Eu^{3+} ions have been excited to higher energy level that lies above the $^5D_0$, then a quick non-radiative (NR) multi-phonon transition occurs to $^5D_0$ emission level ensuing $^5D_0 \rightarrow {}^7F_J$ radiative relaxations by quenching the other emission transitions through ($^5D_3$,$^5D_2$,$^5D_1$) $\rightarrow {}^7F_J$ transitions (not shown in Fig. 8). Thus, the emitted luminescence can be assumed as the cumulative emission of $\Sigma^5D_0 \rightarrow {}^7F_J$ transitions. The multi-phonon relaxation from $^5D_0$ level to its lower lying $^7F_6$ level is disparate due to the huge energy gap of ~ 12,282 cm^{-1}. Since the maximum phonon energy of BiBCEu-G and GCs is of the order ~ 1334.67 cm^{-1}, nearly nine phonons are necessary to bridge the energy gap between $^5D_0$ emission level and $^7F_6$ lower lying level.

The studied samples display intense orange-red emission with CIE (Commission-International de I'Eclairagein) colour coordinates nearly (x = 0.64, y = 0.35), and they are appropriately situated in the orange-red region of CIE diagram described in Fig. 9. These CIE colour coordinates are close to Y_2O_3: Eu^{3+} (x = 0.64, y = 0.34) (KX-YOX, Kasei-Optonix Ltd. Japan), (Y,Gd)BO_3: Eu^{3+} (x = 0.65, y = 0.34) (KX-504, Kasei-Optonix Ltd. Japan) and ideal red emitting source (x = 0.67, y = 0.33) (National Television Standard Committee). They are also close to GC610 (x = 0.625, y = 0.374) [12], $Na_3Gd(PO_4)_2$: Eu^{3+} GCs (x = 0.6233, y = 0.3701) [33] and Al_2O_3: Eu^{3+} ceramic (x = 0.645, y = 0.355) [34].

It is familiar that the intensity of electric dipole (E-D) transition is more responsive and affected by the site symmetry of host where as the intensity of magnetic dipole (M-D) transition is not responsive and do not varies with the site symmetry of host. In case of Eu^{3+}, the $^5D_0 \rightarrow {}^7F_2$ transition is an electric dipole ($\Delta J = 2$) and $^5D_0 \rightarrow {}^7F_1$ is a magnetic dipole ($\Delta J = 1$) in nature. The intensity ratio, $I_R = I_{E-D}/I_{M-D} = I_{(^5D_0 \rightarrow {}^7F_2)}/I_{(^5D_0 \rightarrow {}^7F_1)}$ represents the site symmetry around the Eu^{3+} ions in the given host matrix. Thus, the Eu^{3+} ion can acts as a spectroscopic probe to investigate the local site symmetry of host matrix. Lower the value of I_R higher will be the symmetry around the Eu^{3+} ion in a given host matrix [35]. The value of I_R is found to be 1.80, 1.75 and 1.68 for BiBCEu-G, BiBCEu-GC1 and BiBCEu-GC2, respectively. These results indicate that the site symmetry of the host around the Eu^{3+} ions increases with the increase of crystallization due to the controlled heat treatment. Symmetric environment around the Eu^{3+} ions has been reported for different host matrices in the literature [28, 36–39].

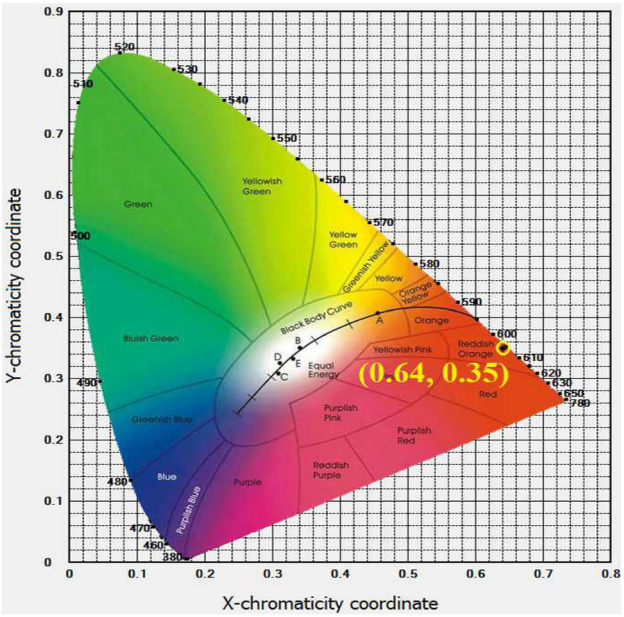

Fig. 9 CIE diagram of BiBCEu-G and GCs

3.4 Judd–Ofelt and radiative parameters

The three phenomenological J-O parameters are the characteristics of RE ions in a specified host and they correspond to the radial wave functions of the $4f^N$ energy levels, the admixing $4f^{N-1}5d$ energy levels and the ligand field parameters that describe the host matrix. In case of Eu^{3+} ion, the J-O parameters have been determined using the relation among $^5D_0 \rightarrow {}^7F_J$ emission transitions and they are used to evaluate the radiative parameters such as radiative emission probability (A_R), radiative luminescence branching ratio (β_R) and radiative decay time (τ_R). The radiative emission rate from the $^5D_0$ upper level to the.^7F_J lower lying levels is given as [8, 9]

$$A_R = \frac{64\,\pi^4\,v^3}{3h\,(2J+1)}\left[\frac{n\,(n^2+2)^2}{9}\right]\sum_{\lambda}\left|\left\langle {}^5D_0\left\|U^{(\lambda)}\right\|{}^7F_J\right\rangle\right|^2 \quad (1)$$

where n is the index of refraction, $\left\|U^{(\lambda)}\right\|$ represents the reduced matrix elements and J is the sum of spin and orbital angular momenta of ground energy level. Though the index of refraction is wavelength dependent parameter, a constant value has been taken to evaluate the various spectroscopic

parameters which cause a negligible deviation in the obtained Ω_λ values. This deviation is mainly due to the small variation in the value of index of refraction in the studied wavelength region, i.e., 580–720 nm. The Ω_λ values have been estimated using the intensities of $^5D_0 \rightarrow {}^7F_J$ emission transitions of Eu^{3+} ion using the relation.

$$\frac{\int I_\lambda \, dv}{\int I_1 \, dv} = \frac{e^2}{S_{md}} \left(\frac{v_\lambda}{v_1}\right)^3 \frac{n\,(n^2+2)^2}{9\,n^3} \Omega_\lambda \left|\left\langle {}^5D_0 \left\| U^{(\lambda)} \right\| {}^7F_\lambda \right\rangle\right|^2 \quad (2)$$

where, $\int I_\lambda \, dv$ and $\int I_1 \, dv$ illustrate the intensity of emission leap at 396 nm excitation (i.e., $^5D_0 \rightarrow {}^7F_\lambda$ (λ = 2,4,6) and $^5D_0 \rightarrow {}^7F_1$ emission transitions, respectively). The parameter S_{md} represents the magnetic dipole line strength of $^5D_0 \rightarrow {}^7F_1$ emission transition. v_1 and v_λ are the energies corresponding to the $^5D_0 \rightarrow {}^7F_1$ and $^5D_0 \rightarrow {}^7F_\lambda$ transitions, respectively. The Ω_λ values have been evaluated considering $\left\|U^{(6)}\right\|^2 \approx 0.0003$ for $^5D_0 \rightarrow {}^7F_6$ transition and zero for other transitions such as $^5D_0 \rightarrow {}^7F_2$ and $^5D_0 \rightarrow {}^7F_4$. The $^5D_0 \rightarrow {}^7F_6$ emission band has peak maximum in near infrared (− 800 nm) and it is not obtained owing to the limitations of measuring instruments. Thus, the Ω_2 and Ω_4 values related to $^5D_0 \rightarrow {}^7F_2$ and $^5D_0 \rightarrow {}^7F_4$ transitions, respectively have been determined using the matrix elements of $\left|\left\langle {}^5D_0 \left\| U^{(2)} \right\| {}^7F_2 \right\rangle\right|^2 = 0.0032$ and $\left|\left\langle {}^5D_0 \left\| U^{(4)} \right\| {}^7F_4 \right\rangle\right|^2 = 0.0023$ [40, 41]. The luminescence branching ratio ($\beta_R = \tau_R \times A_R$) and the radiative decay time ($\tau_R = 1/\Sigma A_R$) have also been obtained using the J-O theory. The values of J-O parameters and some significant radiative parameters of BiBCEu-G and GCs are also summarized in Table 1.

The obtained Ω_2 intensity parameter of BiBCEu-GC2 is comparable to GCLSCAS [42], Eu^{3+}: NAT ceramic [43] and oxyfluoroborate GC [44]. It is found higher than GC400 [45] and lower than Eu^{3+}: Tellurite Ceramic [46], GC24h [11] and TBBS: 2Eu (GC) [47]. A comparison of J-O intensity parameters in various glass–ceramics is given in Table 2. The measured values of branching ratios (β_m) have been obtained using the relative areas covered by emission bands are found close to the β_R (see Table 1). The branching ratio values have been utilized to study the strength of a stimulated emission transition. An emission transition with $\beta_m > 0.50$ possess strong stimulated emission. The measured and predicted values of branching ratios of the order − 0.60 advise that the BiBCEu-GC2 is suitable for intense orange-red laser sources.

The stimulated emission cross-section (σ_e) which is used to identify a laser active media have been evaluated using the following equation.

$$\sigma_e = \frac{\lambda_P^4 \times A_R}{8\,\pi\, c\, n^2\, \Delta\lambda_P} \quad (3)$$

where λ_P represents the peak emission wavelength, c represents the light speed and $\Delta\lambda_P$ represents the effective line-width (or) full width at half maximum (FWHM) of an emission transition. The gain parameters such as band width gain ($\sigma_e \times \Delta\lambda_P$) and optical gain ($\sigma_e \times \tau_m$) have been used to study the amplification of gain medium where RE ions are situated. In current research work, the optical gain is found almost constant, while the band width gain decreases with increase of crystalline environment around the Eu^{3+} ions. The evaluated values of $\Delta\lambda_P$, σ_e, ($\sigma_e \times \Delta\lambda_P$) and ($\sigma_e \times \tau_m$) are also summarized in Table 1. The decrease in σ_e with increase of heat treatment results an intense luminescence in a narrow region. The value of σ_e obtained for BiBCEu-GC2 is comparable to PTBEu glass [48] and higher than RLTB [49] glass.

3.5 Decay time analysis

The luminescence decay profiles of Eu^{3+}: $^5D_0$ metastable energy state in BiBCEu-G and GCs obtained by exciting at 396 nm monitoring the emission at 616 nm ($^5D_0 \rightarrow {}^7F_2$) are displayed in Fig. 10. From the decay profiles one can notice that all the decay curves are well suited for single exponential nature which reveals insignificant non-radiative (NR) losses. The magnitudes of decay time have been determined to be 1.527, 1.534 and 1.594 ms for BiBCEu-G, BiBCEu-GC1 and BiBCEu-GC2, respectively by suitably fitting to single exponential function.

The luminescence quantum efficiency (η) which is the ratio of measured decay time (τ_m) to the radiative decay time (τ_R) is one of the most significant laser characteristic parameter and it is the measure of number of photons emitted per excited ion. The quantum efficiency for Eu^{3+}: $^5D_0 \rightarrow {}^7F_2$ (616 nm) emission transition is found to be 39.97, 40.05 and 41.51% for BiBCEu-G, BiBCEu-GC1 and BiBCEu-GC2, respectively. The value of η obtained for BiBCEu-GC2 (η = 41.51%) is comparable to $BaMoO_4$:-Eu^{3+} GC (46.3%) [10], GC24h (48%) [11] and PTBEu glass (40%) [48]. Based on the experimental results it

Table 1 J-O intensity parameters and radiative properties for $^5D_0 \rightarrow {}^7F_2$ (616 nm) emission transition of Eu^{3+} in BiBCEu-G and GCs

Parameter	BiBCEu-G	BiBCEu-GC1	BiBCEu-GC2
Ω_2 ($\pm$ 0.02 $\times$ 10^{-20}) cm^2	2.66	2.59	2.46
Ω_4 ($\pm$ 0.02 $\times$ 10^{-20}) cm^2	0.35	0.36	0.38
Ω_6 ($\pm$ 0.02 $\times$ 10^{-20}) cm^2	− 0	− 0	− 0
FWHM ($\pm$ 0.05 nm)	10.93	10.60	10.80
A_R ($\pm$ 0.08 s^{-1})	163.80	159.86	157.47
β_R ($\pm$ 0.01)	0.62	0.62	0.61
β_m ($\pm$ 0.03)	0.61	0.62	0.60
τ_R ($\pm$ 0.01 ms)	3.82	3.83	3.84
τ_m ($\pm$ 0.006 ms)	1.527	1.534	1.594
η ($\pm$ 0.01%)	39.97	40.05	41.51
σ_e ($\pm$ 0.01 $\times$ 10^{-22} cm^2)	8.37	8.34	7.94
($\sigma_e \times \Delta\lambda_P$) ($\pm$ 0.01 $\times$ 10^{-28} cm^3)	9.15	8.84	8.57
($\sigma_e \times \tau_m$) ($\pm$ 0.01 $\times$ 10^{-24} $cm^2 s$)	1.27	1.27	1.26

Table 2 Comparison of J-O intensity parameters (Ω_λ) in various GCs

Host matrix		$\Omega_\lambda \times 10^{-20}$ cm^2		Trend
		Ω_2	Ω_4	
BiBCEu-GC2	[This work]	2.46	0.38	$\Omega_2 > \Omega_4$
GCLSCAS	[42]	1.85	4.67	$\Omega_2 < \Omega_4$
Eu^{3+}: NAT ceramics	[43]	2.95	0.39	$\Omega_2 > \Omega_4$
Oxyfluoroborate GC	[44]	2.10	4.05	$\Omega_2 < \Omega_4$
GC400	[45]	1.38	0.84	$\Omega_2 > \Omega_4$
Eu^{3+}: Tellurite Ceramic	[46]	4.30	3.23	$\Omega_2 > \Omega_4$
GC24h	[11]	4.17	2.37	$\Omega_2 > \Omega_4$
TBBS: 2Eu (GC)	[47]	3.21	1.37	$\Omega_2 > \Omega_4$

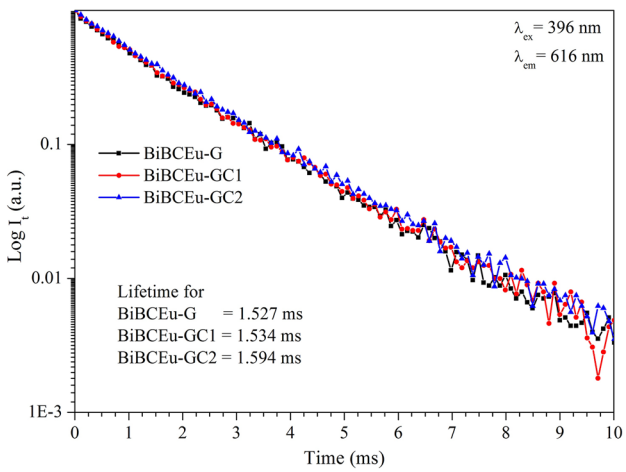

Fig. 10 Luminescence decay profiles of BiBCEu-G and GCs

can be suggestible that the BiBCEu-GC2 has high potentiality to produce intense orange-red luminescence (− 616 nm) when excited at 396 nm radiation.

4 Conclusions

The BiBCEu-G and GCs have been prepared to investigate the crystallization effect on orange-red emission of Eu^{3+} ions. After appropriate heat treatment at 575 °C for 10 h, the $Bi_3B_5O_{12}$ and the CaF_2 nanocrystallites distributed homogeneously among the glassy matrix. Observed intensity ratios of $^5D_0 \rightarrow {}^7F_2$ to $^5D_0 \rightarrow {}^7F_1$ transitions indicate that the symmetry of the host environment around the Eu^{3+} ions improve with the enhancement of duration of heat treatment and hence the crystallization of $Bi_3B_5O_{12}$ and CaF_2 nanocrystallites. Upon 396 nm excitation, the 616 nm emission (Eu^{3+}: $^5D_0 \rightarrow {}^7F_2$) significantly enhanced by the improved crystallization. Obtained results showed that the BiBCEu-GC2 containing 1.0 mol% of Eu^{3+} ions is advisable to design orange-red laser sources.

Acknowledgements

K. Pavani acknowledges the funding by national funds (OE), through FCT—Fundação para a Ciência e a Tecnologia, I.P., in the scope of the framework contract foreseen in the numbers 4, 5 and 6 of the article 23, of the Decree-Law 57/2016, of August 29, changed by Law 57/2017, of July 19 and the project i3N, UIDB/50025/2020 & UIDP/50025/2020, financed by national funds through the FCT/MEC.

Author contributions

BCJ: Conceptualization, Methodology, Validation, Investigation, Writing-Original draft preparation, Writing-Review & Editing, Visualization, Supervision, Project administration, NM: Conceptualization, Investigation, Resources, Writing-Review & Editing, SA: Conceptualization, Investigation, Resources, Writing-Review & Editing, KVR: Conceptualization, Investigation, Resources, Writing-Review & Editing, KP: Conceptualization, Investigation, Writing-Review & Editing, Visualization, Project administration.

Funding

This study is supported by the Fundação para a Ciência e a Tecnologia, UIDB/50025/2020 to K. Pavani.

Data availability

Data will be made available on reasonable request.

Declarations

Conflict of interest The authors declare that they have no conflict of interest.

References

1. A.J. Stevenson, H.S. Brault, P. Gredin, M. Mortier, J. Fluorine Chem. **132**, 1165 (2011)
2. B. Yu, B. Zheng, H. Xia, J. Wang, H. Song, B. Chen, Ceram. Int. **47**, 9668 (2021)
3. K.S. Shaaban, A.M. Al-Baradi, Z.A. Alrowaili, A.M. Ali, M.S. Al-Buriahi, E.A.A. Wahab, J. Mater. Sci. Mater. Electron **32**, 28065 (2021)
4. A.C. Galca, N. Preda, C.E. Secu, C.R. Luculescu, M. Secu, Opt. Mater. **34**, 1493 (2012)
5. B.C. Jamalaiah, G. Viswanadha, J. Eur. Ceram. Soc. **40**, 4578 (2020)
6. A. Herrmann, A. Simon, C. Rüssel, J. Lumin. **132**, 215 (2012)
7. P. Zhili, W. Yongsheng, H. Dawei, M. Xianguo, J. Rare Earths **27**, 338 (2009)
8. B.R. Judd, Phys. Rev. **127**, 750 (1962)
9. G.S. Ofelt, J. Chem. Phys. **37**, 511 (1962)
10. X. Yuhang, Z. Xiangyu, Z. Hongbo, Z. Mengjie, M. Shuo, S. Chunhui, J. Shao, J. Non-Cryst, Solids **500**, 243 (2018)
11. L.M. Marcondes, S.H. Santagneli, D. Manzani, F.C. Cassanjes, G. Batista, V.G. Mendoza, C.R. Cunha, G.Y. Poirier, M. Nalin, J. Alloys Compd. **842**, 155853 (2020)
12. W. Zhang, S. Ouyang, Z. Zhang, Y. Zhang, H. Xia, Ceram. Int. **41**, 14035 (2015)
13. S.H. Tao, D.S. Xun, X.S. Qing, H.L. Li, J.Z. Hong, Chin. Phys. Lett. **21**, 2292 (2004)
14. R.C. Lucacel, I. Ardelean, J. Non-Cryst, Solids **353**, 2020 (2007)
15. S. Rada, M. Culea, M. Neumann, E. Culea, Chem. Phys. Lett. **460**, 196 (2008)
16. E.I. Kamitsos, M.A. Karakassides, G.D. Chyssikos, J. Phys. Chem. **91**, 1073 (1987)
17. A.A. Kharlamov, R.M. Almeida, J. Heo, J. Non-Cryst, Solids **202**, 233 (1996)
18. J.P. Russell, Proc. Phys. Soc. **85**, 194 (1965)
19. A.R. Gee, D.C. ÓShea, H.Z. Cummins, Solid State Commun. **4**, 43 (1965)
20. S. Filatov, Y. Shepelev, R. Bubnova, N. Sennova, A.V. Egorysheva, Y.F. Kargin, J. Solid State Chem. **177**, 515 (2004)
21. A.V. Egorysheva, V.I. Burkov, V.S. Gorelik, Y.F. Kargin, V.V. Koltashev, V.G. Plotnichenko, Phys. Solid State **43**, 1655 (2001)
22. G. George, J. Hayes, C.N. Collins, J.E. Davis, L. Yu, Y. Lin, J. Wen, D. Ila, Z. Luo, J. Alloys Compds. **857**, 157591 (2021)
23. H. Sun, L. Hu, C. Yu, G. Zhou, Z. Duan, J. Zhang, Z. Jiang, Chem. Phys. Lett. **408**, 179 (2005)
24. J.L. Adam, C. Ricordel, J. Lucas, J. Non-Cryst, Solids **213–214**, 30 (1997)
25. V. Nazabal, M. Poulain, M. Olivier, P. Pirasteh, P. Camy, J.L. Doualan, S. Guy, T. Djouama, A. Boutarfaia, J.L. Adam, J. Fluorine Chem. **134**, 18 (2012)
26. Y. Chen, Y. Huang, M. Huang, R. Chen, Z. Luo, Opt. Mater. **25**, 271 (2004)

27. W.T. Carnall, P.R. Fields, K. Rajnak, J. Chem. Phys. **49**, 4450 (1968)
28. B.C. Jamalaiah, N. Madhu, K.V. Rao, G. Viswanadha, D.V.R. Ram, J. Lumin. **223**, 117200 (2020)
29. N.F. Mott, E.A. Davis, *Electronic processes in non-crystalline materials*, 2nd edn. (Clarendon Press, New York, 1979), pp.382–428
30. A. Chakrabarti, A.T.A.R. Molla, J. Am. Ceram. Soc. **101**, 231 (2018)
31. R.E.M. Khaidir, Y.W. Fen, M.H.M. Zaid, K.A. Matori, N.A.S. Omar, M.F. Anuar, S.A.A. Wahab, A.Z.K. Azman, Optik **182**, 486 (2019)
32. Y. Hu, Y. Shen, C. Zhu, S. Liu, H. Liu, Y. Zhang, Y. Yue, J. Non-Cryst, Solids **555**, 120533 (2021)
33. X. Chen, H. Zhang, W. Jia, C. Su, Optik **238**, 166778 (2021)
34. K. Drdlikova, R. Klement, H. Hadraba, D. Drdlik, D. Galusek, K. Maca, J. Eur. Ceram. Soc. **37**, 4271 (2017)
35. K. Binnemans, Coord. Chem. Rev. **295**, 1 (2015)
36. A.M. Babu, B.C. Jamalaiah, T. Suhasini, T.S. Rao, L.R. Moorthy, Solid State Sci. **13**, 574 (2011)
37. S. Todoroki, S. Tanabe, K. Hirao, N. Soga, J. Non-Cryst, Solids **136**, 213 (1991)
38. M.S. Sajna, S. Gopi, V.P. Prakashan, M.S. Sanu, C. Joseph, P.R. Biju, N.V. Unnikrishnan, Opt. Mater. **70**, 31 (2017)
39. H.V. Tuyen, P.V. Do, V.X. Quang, N.T.T. An, L.V.K. Bao, N. Tran, Phys. B **555**, 36 (2019)
40. R.V. Deun, K. Binnemans, C.G. Walrand, J.L. Adam, J. Phys. Chem. Matter **10**, 7231 (1998)
41. M. Dejneka, E. Snitzer, R.E. Riman, J. Lumin. **65**, 227 (1995)
42. R.F. Muniz, D. de Ligny, M. Sandrini, V.S. Zanuto, A.N. Medina, J.H. Rohling, N.B. Aranda, M.L. Baesso, Y. Guyot, J. Lumin. **201**, 123 (2018)
43. B.J. Chen, E.Y.B. Pun, H. Lin, J. Alloys Compds. **479**, 352 (2009)
44. Y. Dwivedi, S.B. Rai, Opt. Mater. **31**, 87 (2008)
45. D. Zhao, X. Qiao, X. Fan, M. Wang, Phys. B **395**, 10 (2007)
46. W. Stambouli, H. Elhouichet, B. Gelloz, M. Férid, J. Lumin. **138**, 201 (2013)
47. M. Walas, M. Lisowska, T. Lewandowski, A.I. Becerro, M. Łapiński, A. Synak, W. Sadowski, B. Kościelska, J. Alloys Compds. **806**, 1410 (2019)
48. M.V.V. Kumar, B.C. Jamalaiah, K.R. Gopal, R.R. Reddy, J. Solid State Chem. **184**, 2145 (2011)
49. S.A. Saleem, B.C. Jamalaiah, A.M. Babu, K. Pavani, L.R. Moorthy, J. Rare Earths **28**, 189 (2010)